

Programming the Energy Landscape of 3D-Printed Kresling Origami via Crease Geometry and Viscosity

Samantha Mora^{1,2}, Nicola M. Pugno^{2,3}, Diego Misseroni^{1*}

¹Laboratory for the Design of Reconfigurable Metamaterials and Structures, Department of Civil, Environmental and Mechanical Engineering, University of Trento, Italy.

²Laboratory for Bioinspired, Bionic, Nano, Meta Materials and Mechanics, Department of Civil, Environmental and Mechanical Engineering, University of Trento, Italy.

³School of Engineering and Materials Science, Queen Mary University of London, UK.

*Corresponding author. Email: diego.misseroni@unitn.it

Origami extends beyond intricate paper creations, envisioning revolutionary engineering applications. While 3D printing has simplified fabricating complex structures, Kresling origami remains predominantly paper based due to the challenge of achieving multistable behavior, especially at a small scale. Our study focuses on investigating modifications to the energy landscape induced by changes in crease geometrical parameters, addressing the effects of viscoelasticity in the creases. The latter aspect is investigated using different rubbery materials with varying relaxation moduli. Considering the limitations of manufacturing techniques, we also provide design insights for crease geometry and distribution, along with photopolymers suitable for fabricating both multi- and monomaterial bistable cells, at both micro- and macro- scales. By leveraging 3D printing and overcoming its material and technological constraints, our goal is to contribute to a deeper understanding of the mechanics of 3D printed materials and broaden their applications into new frontiers.

Keywords: Origami, Metamaterials, Multistability, Multi-Material printing, Viscoelasticity.

1 Introduction

Once origami has surpassed the barrier of being merely decorative folded paper objects, it has become a source of inspiration for creating groundbreaking devices across various engineering fields (1). Kresling origami is currently one of the most studied origami patterns for the development of versatile structures, particularly in the programmable soft robotics area (2–9), highly deployable and energy absorption devices (10–14), and wave control metastructures (15–18). Kresling origami is considered a natural twisted buckling shape that results from the compression of two interacting tubes. This pattern can also be identified in nature, for example, in the bellows shapes found in the abdomen of hawk-moths (19, 20). The intrinsic bistability exhibited by a single Kresling cell, permits the achievement of controlled compliant mechanisms and in the case of coupled Kresling cell modules, multistability (21–27). The material characteristics of the creases play a key role in Kresling origami mechanics, regulating the contraction/expansion process, tailoring the overall stiffness, and leading to mono or bistable behaviour (28). Thus, the creases become essential components for controlling the energy landscape of the Kresling cell. Manual, subtractive and additive manufacturing processes have been used for the fabrication of Kresling structures with materials different than the traditional paper or cardboard. This is mostly done at the macro and meso-scale. Since multi-material 3D printing techniques, such as Material Jetting (MJ), Fused Deposition Modeling (FDM), or Fused Filament Fabrication (FFF), enable a more direct methodology to manufacture complex origami shapes and the use of rigid and flexible materials during a single printing round, their popularity has been increasing among academics and industry. There are current examples that exploit these techniques for the fabrication of Kresling structures, with panels made up of stiffer materials and softer creases that act as hinges. It allows for a smoother transition between an expanded and a compressed state, or vice-versa, by using different photopolymers (29–31) or filaments (32–36). In addition, the use of flexible creases improves the fatigue resistance and life cycle of the Kresling cells (37). Resin-based techniques, such as MJ, offer the possibility to build objects with high precision (layers 16-27 microns), a lower level of anisotropy (<5%), smoother surface finishing, fewer support removal operations, stronger interface bond be-

tween rigid and flexible parts, and a broader range of soft photopolymers for fabricating flexible creases, compared to other multi-material printing processes. These types of soft photopolymers are characterized by a long-range crystalline order, which enhances their mechanical strength and enables tunable deformation responses (38). However, this type of 3D printing photo-resins exhibits an inherent viscoelastic (39) behavior that can lead to a temporary bistability in Kresling cells and a gradual loss of stiffness over time. Consequently, the expected achievement of this mechanical characteristic in theory tends to be compromised in practice, and the Kresling cells return to their initial configuration prematurely. Moreover, the technological limitations of most multi-material 3D printers could restrict the possibility of miniaturizing devices, especially in demanding sectors such as biomedical for the fabrication of drug delivery soft robotics. For instance, the minimum wall thickness is constrained by the nozzle size of extrusion printers in FDM and FFF techniques, typically ranging from 0.25 mm to 1.00 mm depending on the current printer series (40, 41). Regarding MJ, producing strong load-bearing elements with less than 1.0 mm thickness is restricted due to the likelihood of presenting defects (42). Furthermore, the majority of the "micro-scale" printers currently available in the market still utilize a single photo-resin. Therefore, this limitation prevents direct fabrication of Kresling cells with the required difference in stiffness between rigid panels and soft creases, and this feature is essential for facilitating the characteristic contraction/expansion mechanism, as seen in multi-material techniques.

1.1 Motivation and outline

The outcomes of our study provide design insights for programming the energy landscape of 3D printed Kresling cells, counteracting the material and technological limitations in 3D printing. Our goal is to enable the manufacturing of more precise, reliable, scalable and multistable Kresling structures. We explored two main manufacturing approaches: Multi-material and Mono-material. In the multi-material scenario, rigid and rubbery photopolymers are assigned to the panels and creases, respectively. Although the bending of the panels plays a significant role in the folding of non-rigid Kresling cells, as seen in paper-based models, we chose to print the panels using rigid materials to better understand the role of the geometry of the creases on the energy landscape of the Kresling cell. Therefore, the primary folding relies mostly on the flexible, rubbery-like creases.

We initially defined the fundamental geometrical parameters of a cylindrical Kresling cell to achieve theoretical bistability and developed parametric 3D models based on this configuration, as illustrated in Fig. 1A. However, the viscoelastic nature of rubbery photopolymers interferes with practical bistability, causing the cell to prematurely return to its original configuration during the compression/expansion process. Then, we implemented a design strategy that involved gradually reducing the cross-section of the crease geometries. This created peak and valley creases with V+circular shapes, variable widths (w), and internal thicknesses (s_i). A parametric study was conducted to assess the influence of these reductions on cross-section and rotational stiffness, using Reduction Factors (RF) ranging from $0.25 \leq RF \leq 0.80$, as shown in Fig. 1B. These gradual reductions facilitated transitions between bistable (Bi), and monostable (M) behavior, as detailed in the results section 2.

The bistable behavior is related to a Kresling cell whose energy landscape exhibits a second local minimum of energy, and negative force in the load path. We categorized the behavior as monostable when the Kresling cell's load path does not intersect its displacement axis at zero load (43). Despite the involvement of a second local minimum of energy, the sample immediately returns to its original configuration after unloading.

Time-dependent stress-strain responses and energy loss are key characteristics of viscoelastic materials, which exhibit residual strain that recovers over time, allowing the material to return to its original state. This results in temporary bistability, particularly in structures with snap-through behavior. Once stress relaxation occurs, stability is lost, and the structure gradually returns to its initial configuration. In our second analysis, we evaluated these effects in bistable multi-material Kresling cells with rubbery photopolymer creases of varying relaxation moduli. In the numerical simulations, we considered elasto-plastic and visco-hyperelastic models with 3D hybrid formulation elements to accurately capture the mechanical behavior of 3D-printed rigid and rubbery photopolymers, respectively. This approach offers a more realistic alternative to traditional 2D origami models, particularly for materials such as paper or thin polymeric sheets.

We experimentally validated the load paths and energy landscapes obtained numerically by testing 3D-printed Kresling cells fabricated using the Polyjet technique. In addition, we performed microscopic characterization of the rubbery creases to assess potential dimensional discrepancies between the CAD model and actual printed dimensions, as illustrated in Fig. 1C. Lastly, we

explored alternative designs for a mono-material bistable cell, as depicted in Fig. 1D, aimed at microfabrication. The stiffness differences between creases and panels are achieved through geometric reductions, including voids along the peaks and valleys. Furthermore, we also investigated the effects of various 3D printing photo-resins on Kresling multistability and the programmability of monostable Kresling assemblies through crease stiffness distribution.

2 Results

2.1 Parametric study of creases geometry for Bistability

First, we selected the following initial sizing configuration for the parametric design of 3D Kresling cells, shown in Fig. 1A: polygons with $n=6$ sides, initial relative angle $\theta_o = \pi/6$, and an aspect ratio $h_o/r=1.75$, as detailed in sections S.1.1 and S.1.2 of Supplementary Materials and Methods. Initially, we analyzed Kresling cells with intact crease cross-sections. The results showed that their bistability was compromised by a sudden return to the initial configuration, attributed to the viscosity of the rubbery creases (as further explained in the Supplementary Text S.2.1).

As a design strategy to achieve bistability and program energy landscapes, we conducted a parametric study to assess how gradually reducing crease cross-sections influences the energy landscape. The geometrical changes illustrated in Fig. 1B were proposed based on the following procedure: The upper V-shape remained constant, preserving the crease width w , while the bottom part was gradually reduced by considering a variable cutting radius s_c . It encompasses a circumference with its center at the extreme vertex o . Using imposed reduction factors, denoted as RF , we can control the decrease of the parameter s_c relative to the limiting crease radius r' , and thereby determine the extent of crease cross-section reduction. Accordingly, we can define the reduction factor as: $RF = s_c/r'$.

We then introduced a new geometrical parameter corresponding to the internal thickness s_i . This term represents the difference between the external thickness s and the variable cutting-radius s_c , which depends on the selected reduction factor RF . As the RF values decrease, the generated creases exhibit smaller internal thickness s_i and these gradual reductions can be quantified as the ratios of the reduced to intact cross-sections, \tilde{A}/A , and their corresponding rotational stiffness,

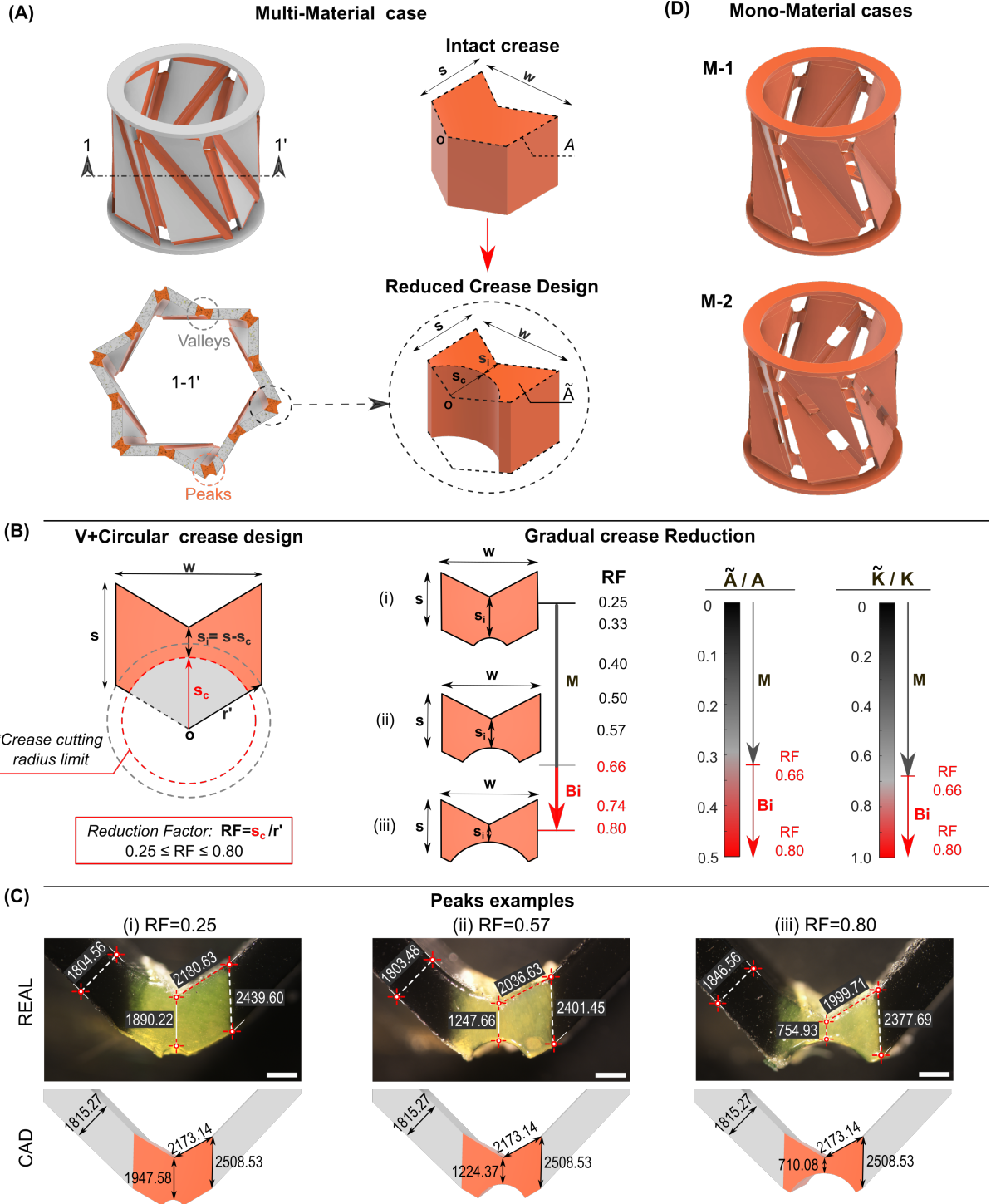


Figure 1: 3D models of the Kresling cell. (A) Multi-material (MM) with crease design cases. (B) Crease cross-section gradual reductions derived from the former intact creases cross-sections, A , with a variable width-thickness ratio w/s , an internal thickness s_i obtained from cutting radius s_c and reduction factors RF . Here, \tilde{A} and A represent the reduced and intact cross-sections, respectively. Similarly, \tilde{K} denotes the rotational stiffness of the reduced cross-sections, while K corresponds to that of the intact cross-sections. (C) Comparison between 3D printed creases dimensions taken from microscope images and CAD files of case C8 with gradual reductions. Units: microns. Scale bar: 1 mm. (D) Mono-material cases M-1 and M-2.

\tilde{K}/K . Here, the reduced cross-sections and corresponding rotational stiffness are denoted by \tilde{A} and \tilde{K} , respectively, while the intact cross-section and its rotational stiffness are denoted as A and K .

As a result, the proposed variable creases geometry consists of a combined V+circular typology, yielding a series of Kresling cell cases to be analyzed in terms of the parameters: w , RF , s_i , and s . Thereby, we introduced eleven main cases, C1 to C11, derived from the variation of the width with respect to the external thickness, expressed as the ratio $w/s=0.50, 0.60, 0.75, 0.90, 1.07, 1.20, 1.35, 1.50, 1.65, 1.80, 2.00$. The gradual reductions applied to each of the main cases are represented by the variations in internal thickness s_i , which directly depend on the reduction factors, denoted as $RF=0.25, 0.33, 0.40, 0.50, 0.57, 0.66, 0.74, \text{ and } 0.80$. This process subdivided each crease case into eight sub-cases, each corresponding to one of the specified RF values. The load paths and stored energy landscapes of the generated geometrical combinations were obtained through numerical simulations, as detailed in Supplementary Text [S.2.2](#), using a multi-material approach. A rigid photopolymer (VB), modeled as an elasto-plastic material, was assigned to the panels. A rubbery photopolymer (DM60), modeled as a visco-hyperelastic material, was assigned to the creases. For this, we incorporated viscoelastic parameters into its characteristic hyperelastic behavior, such as the Prony series coefficients (g_i, τ_i) and relaxation moduli ($G(t)$), as explained in sections [5.3](#), and [S.1.3](#) of Supplementary Materials and Methods. Then, the effect of the gradual reduction of the creases on the energy landscape was evaluated based on the variation of the width w and internal thickness s_i with respect to the external thickness s , denoted as the ratios w/s and s_i/s , respectively.

Thereafter, in Fig. [2A](#), we show which geometrical combinations exhibited a bistable, or monostable behavior, along with their rotational stiffness \tilde{K} , estimated using the bending formulations of an incompressible elastic Neo-Hookean block (44) (as detailed in Supplementary Text [S.2.3](#)). For instance, the Kresling cells that satisfied the bistability criteria were made of wider creases ($1.07 \leq w/s \leq 2.00$) and designed with greater cross-section reductions ($0.05 \leq s_i/s \leq 0.58$). The latter were generated by reduction factors relying on the range $0.66 \leq RF \leq 0.80$. Such reduction factors enabled the creation of creases with the thinnest internal thicknesses s_i , resulting in the highest decrement of cross-section and rotational stiffness up to $\tilde{A}/A=0.50$ and $\tilde{K}/K=0.90$ compared to the corresponding intact creases, as shown in Fig. [1B](#). Therefore, this confirms that as the crease becomes less stiff, it gains enough flexibility to ensure the achievement of bistability. On the other

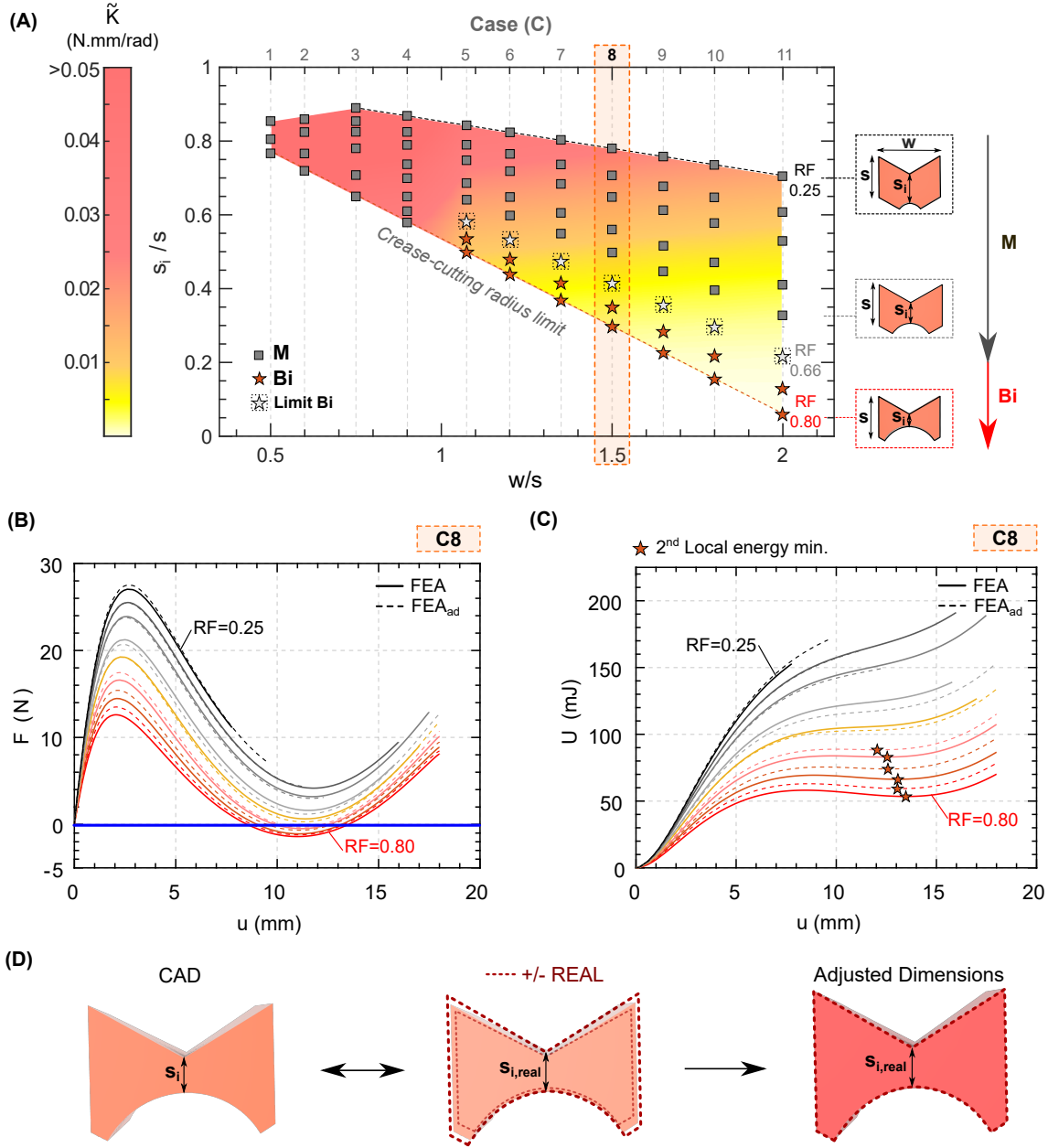


Figure 2: Influence of the creases geometrical parameters on the energy landscape. (A) Parametric study of creases to evaluate the achievement of bistability (Bi), or monostability (M), in terms of the variation of width (w) and internal thickness (s_i) with respect to the external thickness (s), reduction factors (RF) and Rotational Stiffness (\tilde{K}). The crease-cutting radius limit determines the range of reduction factors necessary to maintain a circular shape at the lower part of the crease. 'Limit Bi': boundary between bistability and monostability determined experimentally. Results are based on Kresling cells at 1:1 scale (x1). (B) Load paths and (C) stored energy (U) landscapes of case C8 ($w/s=1.50$) at 3:1 scale (x3). The corresponding curves are presented in the following order RF : 0.25, 0.33, 0.40, 0.50, 0.57, 0.66, 0.74, and 0.80. (D) Iterative process to adjust CAD dimensions, verify discrepancies with the real dimensions of 3D-printed Kresling cells, and determine the corresponding adjusted load paths (FEA_{ad}).

hand, creases designed with reduction factors above $RF=0.66$ reached greater internal thickness (s_i) values. They tend to increase the restoring force values of the respective Kresling cells, gradually moving them away from zero. Therefore, they are unable to achieve bistability and are prone to show a monostable behavior instead. Thus, we determined a possible limit for achieving bistability from the combinations with $RF \geq 0.66$, as shown in Fig. 2A.

In an extreme scenario, when the width versus external thickness ratio is below $w/s \leq 1.07$, the creases tend to be narrower and very rigid, falling into a mono-stable category, and when they presented higher s_i values, the stored energy values also increased. In general, we observed that Kresling cells exhibited monostable behaviors when they are formed by stiffer creases. These crease configurations reached reduction ratios of approximately $\tilde{A}/A \leq 0.30$ for cross-sections and $\tilde{K}/K \leq 0.70$ for rotational stiffness. Moreover, we analyzed the load paths and the corresponding stored energy obtained numerically for the intermediate case C8 ($w/s=1.50$), as shown in Fig. 2B, and Fig. 2C. We compared two types of numerical simulations, the first considering the exact cross-section dimensions from the CAD file and the second with the adjusted dimensions obtained from the microscope characterization, indicated as FEA and FEA_{ad}, respectively. We also observed that a second local minimum of energy was reached when the creases presented gradual reductions between the range $0.35 \leq s_i/s \leq 0.40$ corresponding to the already mentioned reduction factors $0.66 \geq RF \geq 0.80$.

2.2 Scalability and experimental validation

Furthermore, we observed through numerical simulations that the load paths of the analyzed Kresling cells can be scaled. For instance, Fig 3A shows that the position of the second local minimum of energy of the C8 $RF=0.80$ Kresling cell, at a 1:1 scale (x1), varies from a displacement $u=4.53$ mm, to 9.06 mm at a 2:1 scale (x2) and 13.59 mm at a 3:1 scale (x3). This fact demonstrates that scaled Kresling cells maintained the expected bistable behavior at the same geometrical proportions with respect to 1:1 scale (x1). Thus, Kresling cells can be scaled to meet manufacturing requirements across different length scales, from microfabrication to large-scale additive manufacturing. In the present study, Kresling cells for the C8 case were fabricated using the PolyJet technique at a 3:1 scale (x3) for the corresponding experiments, as detailed in section 5.4. This scale ensures feasible

printing, as the internal thickness dimensions s_i , fall within the PolyJet manufacturing limits of 0.6–1.0 mm.

The experimental setup for the compression tests is illustrated in Fig. 3B. The experiments were performed by imposing a displacement u at one side of the sample and leaving free the rotation in the opposite side, as detailed in section 5.5. During the test we monitored the applied displacement u against the measured restoring force F . Moreover, the achievement of bistability is highly sensitive to geometric variations in crease parameters, such as width w and internal thickness s_i . The existent differences between the exact (CAD) and the real dimensions of the 3D printed Kresling cells are attributed to the inherent loss of dimensional accuracy of the 3D printer in use.

Through a microscopic characterization (further explained in sections 5.6 and S.1.10 of Supplementary Materials and Methods), we estimated a mean percentage error, M_{PE} (%), between the exact and the real dimensions of the analyzed creases and panels from a sample corresponding to the case C8. In this example, the internal thickness s_i dimensions exhibited an mean percentage error in the range: $-25 \leq M_{PE} (\%) \leq 10$, where negative values imply higher real measures than the CAD models. This error range represents a small difference between the exact dimensions and the real dimensions of the creases, and corresponds to the expected dimensional accuracy of a J750 Polyjet 3D printer, which is commonly about %10. Therefore, we primarily relied on the load paths obtained from the numerical simulations (FEA) using the exact dimensions from the CAD file geometry for their respective experimental validation, as shown in Fig. 3C, D and E.

Subsequently, we experimentally confirmed that C8 case samples with reduction factors in the range $0.25 \leq RF \leq 0.57$ exhibited monostability, as illustrated in Fig. 3C. These cases corresponded to creases with internal thickness s_i greater than the manufacturing limit of 1.0 mm. The effect of crack formation during the experiments on these thicker creases was minimized. For this reason, the numerical load paths (FEA) closely matched those obtained experimentally (EXP). In Fig. 3D, the experiments from C8 cases with $0.74 \leq RF \leq 0.80$ validated the bistable behavior observed in the corresponding Kresling cells at a 1:1 scale, as described in Fig. 2A.

However, some discrepancies were observed in the load path region where a change in the sign of the load was expected. This may be attributed to the fact that these narrow creases, with thicknesses below the manufacturing limit of 0.6 mm, are prone to develop longitudinal cracks that dramatically reduce their stiffness. In addition, the load path corresponding to the configuration

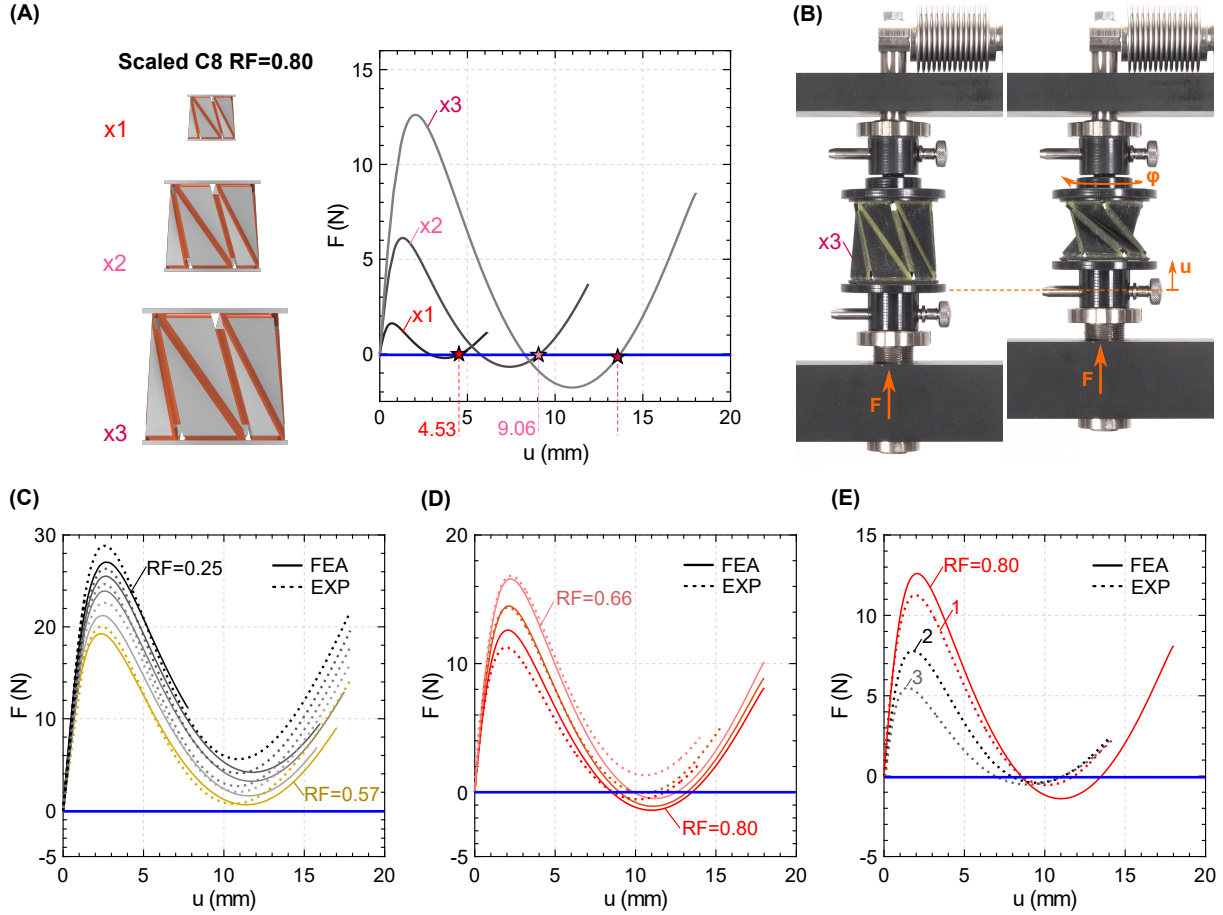


Figure 3: Scalability and experiments on multi-material 3D printed Kresling cells. (A) Observed scalability in Load paths and in the position of the second local minimum of energy on Kresling cells, at a 1:1 (x1), 2:1 (x2) and 3:1 (x3) scales. (B) Experimental Setup for multi-material 3D printed Kresling cells at 3:1 scale, designed to impose a vertical displacement u corresponding to a restoring force F , with free rotation at one end. (C-E) Comparison between Numerical and Experimental tests performed on case C8 with: (C) $RF = 0.25, 0.33, 0.40, 0.50$ and 0.57 . (D) $RF = 0.66, 0.74,$ and 0.80 . (E) Effect of the degradation of the rubbery crease cross-sections on the load path after performing three sequential experiments on the same sample (C8, $RF=0.80$ creases made of DM60).

with a reduction factor of $RF = 0.66$ may represent the actual limit between bistability and monostability, denoted as 'Limit Bi' in Fig. 2A. Its experimental load path tends to remain above zero, making it difficult to confirm whether the condition for achieving a second local minimum of energy is truly satisfied, as shown by the corresponding numerical load path. A summary of the experiments, including hands-on experimental validation of bistability, is presented in videos S1 and S2. Furthermore, we observed that sequential compression tests can induce degradation in the rubbery photopolymer, resulting in longitudinal cracks along the creases, particularly in areas with

cross-sectional dimensions smaller than 0.6 mm. To investigate this, we performed the compression experiment three times on the same samples.

Gradual decreases in the load values achieved for sample $RF = 0.80$ were detected across experimental curves denoted 1, 2, and 3, as shown in Fig. 3E, along with additional details in video S3 and supporting Fig. S24. We determined that approximately 30% and 50% of the load capacity achieved in test 1 was lost after tests 2 and 3, respectively.

2.3 Effects of creases viscosity on bistability

In a second parametric study, we focused on the effects of viscosity on the bistability and stored energy in Kresling cells composed of rubbery creases while preserving the same rigid panels. Specifically, we analyzed the configurations of creases from cases C8 to C11, which led to bistability during the first parametric study described in section 2.1. Those creases were modeled exclusively with the rubbery material DM60, which has a relaxation modulus of $G_{60}=0.220$ MPa. The selected groups of creases are located within the following geometrical ranges: $0.05 \leq s_i/s \leq 0.41$ and $1.50 \leq w/s \leq 2.00$, as shown in Fig. 4A. We obtained the corresponding numerical load paths and energy landscapes using various rubbery photopolymers characterized by different relaxation moduli and viscosity with respect to DM60, including AG30 ($G_{\infty}=0.7G_{60}$), DM70 ($G_{\infty}=1.4G_{60}$), DM85 ($G_{\infty}=2.6G_{60}$), and DM95 ($G_{\infty}=3.9G_{60}$), as detailed in Supplementary Text S.2.4. Their viscoelastic properties, such as relaxation modulus ($G(t)$) and Prony parameters (g_i, τ_i), were determined experimentally (see Section S.1.6 of Supplementary Materials and Methods for more details). As a result, Fig. 4A summarizes whether bistability is preserved in the geometrical configurations analyzed under various levels of relaxation modulus and viscosity. In addition, bistability was numerically evaluated over different time scales, considering the initial (τ_i^*), short- (τ), and long-term ($n\tau$) relaxation times exhibited by the visco-hyperelastic materials analyzed, as indicated in Fig. 4B.

Thus, we observed that Kresling cells composed of creases with a lower relaxation modulus, characterized by the softest photopolymers AG30, DM60, and DM70, remained in bistable behavior in the majority of cases and in all the analyzed time scales. Configurations whose reduction factors are in the range within $0.74 \leq RF \leq 0.80$ can also achieve bistability with rubbery materials having

an intermediate relaxation modulus, such as that of DM85. However, in cases where geometrical configurations are at the limit of achieving bistability, which are generated with a reduction factor $RF=0.66$ and when using DM85, a monostable scenario occurred. On the other hand, we inferred that at the highest relaxation modulus and viscosity, for instance DM95 material, the Kresling cell tends to exhibit monostability in most cases. Consequently, we estimate that as the rubbery material in the creases becomes more highly viscous, with a high relaxation modulus, the load values consistently stay above zero, and the sample tends to return to its initial state, compromising a bistable behavior.

2.4 Experiments on Kresling Cells with variable visco-hyperelastic creases

We selected the configurations of the case C8 $RF=0.80$ to experimentally validate their bistable behavior previously described in Fig. 4A. For this, we compared their numerical and experimental load paths and stored energy landscapes, as illustrated in Fig 4C. The fabrication of the samples and the experiments were done as detailed in sections 5.4 and 5.5, respectively. We confirmed experimentally that bistability is maintained by Kresling cells made of creases with the less stiff rubbery materials and characterized by lower relaxation moduli, such as AG30, DM60, DM70, and the intermediate, DM85. Similarly, Kresling cells with creases made of DM95, which has the highest relaxation modulus among the analyzed rubbery materials, lost the ability to achieve bistability in practice. Instead, the Kresling cell transitioned to a monostable scenario, where the load values tend to deviate further from intersecting the displacement axis at zero force. Then, a corresponding rise in stored energy is observed without reaching a second local minimum of energy. This occurs despite the fact that the geometrical design favors bistability when using softer materials with lower relaxation moduli. We can attribute this to the fact that the rubbery material DM95 is more likely to exhibit higher viscosity than the other photopolymers and retain stiffness over time, making even the folding of the Kresling cell more difficult. Consequently, we observed that variations in relaxation modulus can aid in tuning the energy landscapes, as well as modifying the geometrical parameters of the creases.

The experiments were conducted similarly to those described in section 2.2 and included hands-on experimental validation of bistability, as shown in video S4. We also detected crack

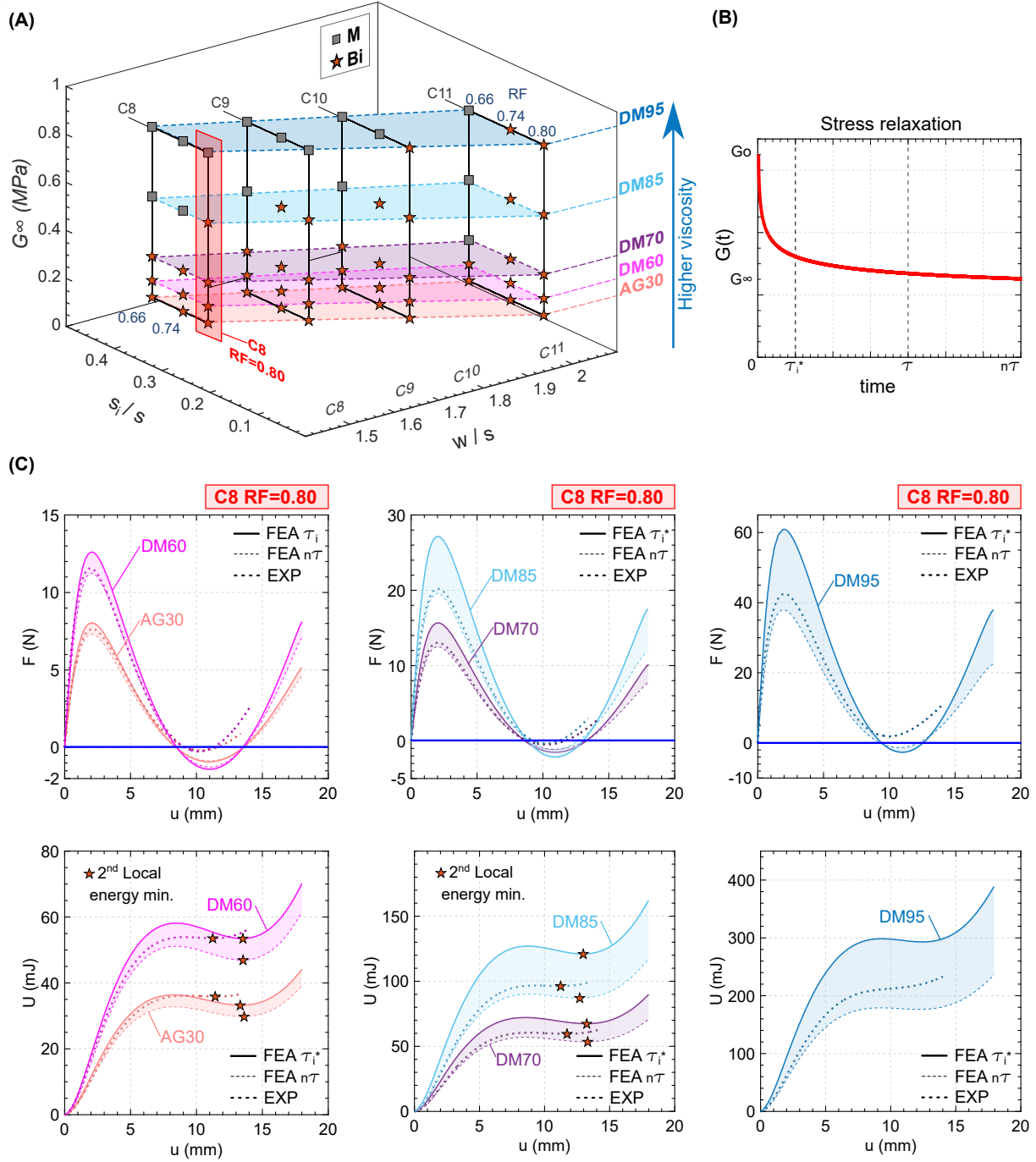


Figure 4: Visco-hyperelastic effects on the achievement of bistability. (A) Parametric study to assess bistable Kresling cells with creases made of rubbery materials (AG30, DM60, DM70, DM85 and DM95) with different viscoelastic properties in terms of relaxation modulus G_∞ , for Cases C8, C9, C10, and C11 designed with reduction factors within the ranges $0.66 \leq RF \leq 0.80$. Results of Kresling cells at 1:1 scale ($\times 1$). (B) Experimental relaxation curve. Times τ_i^* , τ and $n\tau$, respectively considered for the numerical analysis of viscosity effects. Experiments were performed at a test speed which correspond to a relaxation time $\tau_i^*=180$ s. (C) Numerical and experimental load paths, along with stored energy landscapes (U). Results for C8 RF=0.80 cells at a 3:1 scale ($\times 3$), with rubbery creases exhibiting different relaxation moduli. Filled regions include FEA simulations within the range $\tau_i^* \leq \tau \leq n\tau$.

initiation along the creases made of other rubbery materials different from DM60, including AG30, DM70, DM85 and DM95, in the tested Kresling cells. This affected the accuracy of the experimental load paths with respect to the corresponding numerical counterparts, as we observed in the experiments shown in Fig. 3D. Likewise, degradation in the creases was noted after testing each sample consecutively three times, representing a technological limitation related to the use of rubbery photopolymers with very small cross-sections (≤ 0.6 mm), as further detailed in supporting Fig. S33.

2.5 Mono-material cells

In the context of the multi-material 3D printing approach, the compression/expansion process of Kresling cells, as well as the achievement of bistability, becomes feasible by combining the bending of rigid panels and rubbery creases. In the case of using a single material, we propose a strategy in which we segmented the creases and create voids along the full volume of the valleys (V_{vf}), and peaks (V_{pf}), as shown in Fig. 5A and B. This difference in volume contributed to reduce the stiffness of the creases with respect to the panels. Then, the analyzed Kresling cells, denoted as M-1 and M-2, are designed with the geometrical configuration of case C11 RF=0.80. We selected this configuration because it potentially exhibits bistability, independently of the viscoelastic properties of the creases materials, as described in Section 2.3. The variable volume of the valley creases is denoted as V_v . In the M-1 case, where the number of voids along the valleys is zero, and their volume is $V_v = V_{vf}$. In M-2 case, the number of voids along the valleys is 2, and their volume is equal to $V_v = 3/5 V_{vf}$.

In both Kresling cell cases M-1 and M-2, the reduction of the peaks volume was also considered as a minimum fraction of their respective full volume, denoted as $V_p = 2/7 V_{pf}$. The remaining small amount of material that forms the peaks, only contributes to the connection between the panels. Thus, we simplify the analysis by regarding the volume of the valleys V_v with their voids inclusions, as the sole variable of analysis. The load paths and energy landscapes corresponding to M-1 and M-2 cases are shown in Fig. 5C and D. They indicate that both Kresling cells, made completely of rubbery photopolymers such as Origin 402, IP-PDMS, and DM95, exhibited a monostable behavior. In addition to these materials, the use of photopolymers with a stiffness of around 600 MPa, like UTL,

suggests that monomaterial Kresling cells can also achieve bistability. This type of photopolymers are used in micro-printing being characterized by high-flexibility and toughness, suitable for snap-fits or similar fixtures. Additional results with rubbery photopolymers, including DM60, DM70, and DM85, are presented in Supplementary Text [S.2.5](#) - Fig. [S11](#).

2.6 Programmable Monostable Kresling Assemblies

The variation of geometrical parameters in Kresling cells, such as initial relative angle θ_o and the aspect ratio between the initial height and the polygon's radius h_o/r , can lead to programmable energy absorption levels. We analyzed the following mono-stable Kresling cell configuration: number of polygon's sides $n=8$, $\theta_o = 45^\circ$, and $h_o/r=0.40$, determined using the same criteria as the previously analyzed configuration with $n=6$. Next, 3D parametric Kresling cells were designed and coupled in chiral configurations to form multi-story cylinders with five stories ($\#stories=5$). In this analysis, we aimed to explore the crucial role of crease stiffness in the compression/expansion process and storing energy in multi-story and monostable Kresling cells.

These structures were numerically analyzed in Abaqus/CAE standard to determine their load paths and energy landscapes during compression, as detailed in section [5](#), and were validated experimentally, as described in section [5.5](#) and video S5. A maximum vertical displacement $u=20\text{mm}$, was applied at the top, while the bottom is fixed, as shown in Fig. [5C](#). The Kresling multi-story cylinders were designed for fabrication using multi-material 3D printing, with rigid panels (VB), and creases made of softer (DM60) and stiffer (DM95) rubbery materials. Thereafter, we generated three different cases to specifically evaluate the influence of creases with variable stiffness: (i) creases made entirely of the softer rubbery material DM60 across all five stories, (ii) stiffer creases in the even stories (DM60-DM95-DM60-DM95-DM60), and (iii) stiffer creases in the odd stories (DM95-DM60-DM95-DM60-DM95).

During the folding of the multi-story cylinders, the numerical load paths were tracked until the contact between panels started, reaching a displacement in the range of $12\text{ mm} \leq u \leq 16\text{ mm}$. We calculated the stored energy at these points. Using the value from case (i) as a reference, we observed increases of 59.15% and 139.05% with the inclusion of stiffer creases, as seen in cases (ii) and (iii), respectively. Moreover, considering the intermediate stories 2, 3, 4 as points of analysis,

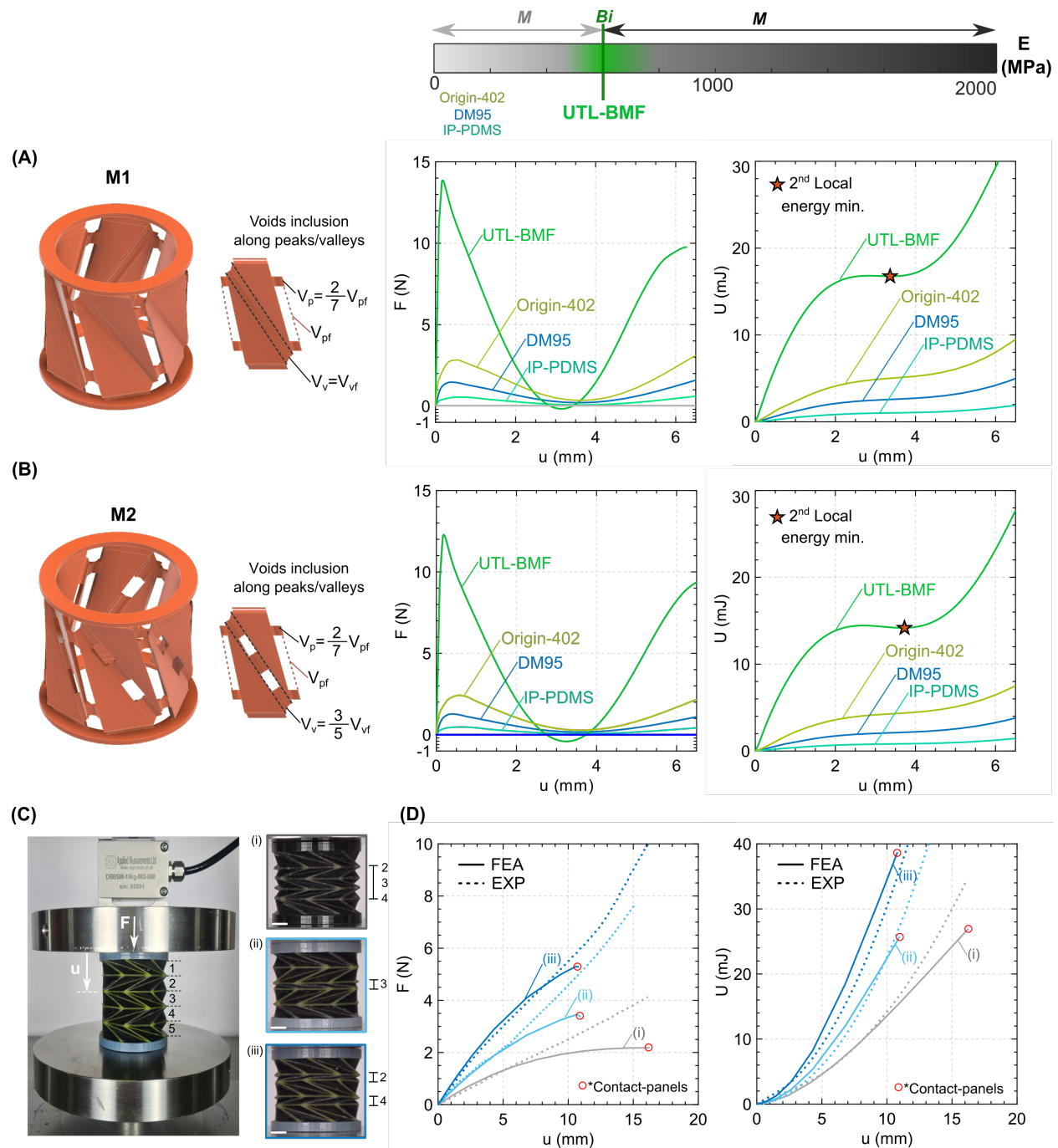


Figure 5: Load paths and stored energy landscapes of monomaterial Kresling cells and programmable Kresling assemblies. (A) M-1, and (B) M-2 cases. Materials with intermediate stiffness tend to achieve bistability (Bi). Results of Kresling cells at 1:1 scale. (C) Compression test and folding process of cases (i) All the creases DM60, (ii) Stiffer creases (DM95) in the even stories, and (iii) Stiffer creases (DM95) in the odd stories. The number of folded stories at a displacement $u \approx 12$ mm is indicated. (D) Numerical (FEA) and experimental (EXP) results. The numerical simulations stopped at the first contact among panels.

we observed that all the stories are folded uniformly in the case (i), where creases are made of the same material DM60. On the alternating creases stiffness cases, stories with creases made of softer material tended to be folded first than their rigid counterparts. For instance, the odd story 3 (DM60) in case (ii), was folded first than the even stories 2 and 4 made of stiffer material (DM95) and vice-versa in case (iii), as described in Fig. 5D. Hence, we proposed another approach for the programmability of stored energy and to control the localized deformation of specific stories during the folding process of multi-story Kresling structures. Therefore, we aimed to provide design hints for 3D printed structures that could potentially be employed in programmable motion and damping devices.

3 Discussion and Limitations

Starting with a Kresling cell configuration ($n=6$, $h_o/r=1.75$, $\theta_o = \pi/6$), along with the proposed gradual reduction of the creases cross sections, we conducted numerical simulations to obtain the corresponding load paths and energy landscapes. Traditional modeling approaches for Kresling structures typically involve thin-shell elements primarily intended for physical prototypes made from paper-based or thin polymer sheets. However, using 3D hybrid-modified elements enabled us to incorporate visco-hyperelastic models, providing a more realistic mechanical response for viscous and nearly incompressible materials, such as the flexible photopolymers used in 3D printing. Under the assumptions of paper-based models, such as constant crease cross-sections and zero viscosity, predictions of mechanical behavior differ when applied to 3D-printed Kresling cells. For example, the design of an intact rubbery crease is more likely to not exhibit the theoretically predicted bistability. For multi-material 3D printing Kresling cells, we established a range of geometrical parameters, including width-to-external thickness ratio w/s , internal thickness s_i , and reduction factor RF , leading to parametric design process to obtain bistable cells. Based on the results of the parametric study, we have confirmed that the geometry of the creases is influential when aiming a specific load path.

Particularly, when the crease width w exceeds a ratio $w/s \geq 1$, the energy landscapes of the multi-material 3D-printed Kresling cells can be significantly controlled by modifying the internal thickness s_i using imposed reduction factors RF , while maintaining the same width w . For

example, we demonstrated that the internal thickness s_i is a critical factor in achieving bistability. Specifically, values in the range $0.05 \leq s_i/s \leq 0.30$ generated by reduction factors RF between 0.74 and 0.80, ensure bistability while reducing the cross-section relative to the intact cross-section by an approximate ratio of $0.50 \leq \tilde{A}/A \leq 0.80$. Consequently, the rotational stiffness of the reduced creases relative to the intact crease decreases to a range of $0.80 \leq \tilde{K}/K \leq 0.90$, ensuring the flexibility required for bistable Kresling cells. In contrast, Kresling cells generated with RF values above 0.66 tended toward monostable behavior in practice. In these cases, we observed that the experimental load path remains above zero, which differs from the numerical counterpart's prediction. Furthermore, we noted that, after applying a compressive load to the Kresling cell, it returned to its initial configuration more quickly, as shown in video S2. Thus, we confirmed that bistability was not achieved in practice.

For this reason, we established a reduction factor $RF=0.66$ as a geometric limit for determining bistability. This discrepancy may be due to slight increases in cross-sectional dimensions resulting from printing accuracy, potentially leading to a greater thickness, s_i , and closer to that of the next case with $RF = 0.57$. Although taking measurements along the crease length is complicated due to the complex geometry of the Kresling cell, the fact of having such a greater crease thickness is confirmed by the microscopic measurements we performed along an horizontal slicing plane that cuts the Kresling cell at the mid-height.

We numerically and experimentally determined how the achieved bistability is affected by the visco-hyperelastic behavior characteristic of rubbery 3D printing materials. For example, in the particular case of C8 Kresling cells with creases made of rubbers with lower (AG30, DM60, DM70) and intermediate (DM85) relaxation moduli preserved bistability. Considering DM60 relaxation modulus as $G_\infty=1.0G_{60}$, we have AG30 ($G_\infty=0.7G_{60}$), DM70 ($G_\infty=1.4G_{60}$) and DM85 ($G_\infty=2.6G_{60}$). In contrast, when the creases were characterized by a higher relaxation modulus such as the case of DM95 material ($3.9 G_{60}$), the Kresling cells transitioned towards a monostable behavior. Our numerical simulations also predicted that bistability is preserved over different time scales corresponding to the initial (τ_i^*), short- (τ), and long-term ($n\tau$) relaxation times. Since numerical simulations showed that the energy landscapes did not vary significantly for relaxation times higher than τ_i , we decided to perform them a test speed which correspond to a relaxation time $\tau_i^*=180$ s. This choice allows for efficient characterization while avoiding unnecessary long-term testing, as

the observed bistability remains over time. When comparing visco-hyperelastic creases made of different rubbery materials, the viscoelastic component, specifically the difference in relaxation modulus, appeared to have a greater effect on achieving bistability than the time scale of analysis. Furthermore, these results suggest that specific geometrical parameters leading to creases with smaller cross-section thickness s_i , such as those generated with a reduction factor $RF=0.80$, play a more significant role in the achievement bistability and programming the energy landscape, counteracting the inherent viscoelastic effects.

In the case of a monomaterial approach, the geometrical designs with the narrowest creases (especially those generated with a reduction factor $RF=0.80$) were selected, as they provide the highest rotational stiffness reduction $\tilde{K}/K \approx 0.90$ and flexibility. Our design strategy was based on variations in stiffness along the creases, achieved through the inclusion of voids in the peaks and valleys, which facilitated the compression and expansion processes of the Kresling cell. Regardless of the material used, we also evidenced that decreasing the volumes of the creases by including more voids along the valleys, can modify the energy landscapes resulting in lower stored energy values. These differences can be observed by comparing the energy landscapes corresponding to the cases M-1 in Fig. 5A and M-2 in Fig. 5B. For example, considering both cases made of UTL resin, M-1 and M-2, their achieved total stored energy values were $U=32$ mJ and $U=26$ mJ, respectively. This means that the inclusion of two voids along the valleys, corresponding to the fraction $V_v=3/5 V_{vf}$, can result in a decrease of 18.75% in the total stored energy.

Since rubbery photopolymers exhibit low tensile instantaneous relaxation moduli between $1.0\text{MPa} \leq E_o \leq 10\text{MPa}$, the effect of their visco-hyperelastic properties on preserving bistability is almost not mitigated without the interaction with stiffer panels. On the other hand, very rigid photopolymers led to earlier failure, tending to present a brittle behavior, and the folding mechanism is limited. For this reason, materials with intermediate stiffness values can be an alternative for achieving bistability. We have confirmed this fact by analyzing a Kresling cell composed of UTL resin (45), with a Young's Modulus around $E \approx 600$ MPa, where bistability was observed. Therefore, it opens the possibility of miniaturizing bistable Kresling cells using a single material. These configurations can be used to fabricate downscaled Kresling cells, even at the micro-scale, thereby overcoming the dimensional limitations of traditional 3D printing technologies.

In addition, we investigated the role of creases in monostable Kresling assemblies. Using a

multi-material printing approach, we evaluated and fabricated Kresling structures with variable stiffness assigned to the creases in even and odd stories. For instance, during the folding process, deformation occurs first in the stories with softer creases, such as those made of DM60, and later in the stiffer ones made of DM95. This approach facilitates the control and programming of the energy landscape. Notably, we also achieved an increase of up to approximately 140% in stored energy by including stiffer creases.

3.1 Limitations

We validated the numerical predictions experimentally, considering manufacturing limitations to prevent defects at the time of fabricating 3D-printed parts. Dimensional constraints due to technological limitations restrict the size of 3D-printed multi-material Kresling cells that can be tested. In the case of the PolyJet technique, load-bearing elements with cross-sections smaller than 0.6 mm tend not to cure well and may exhibit defects during the photopolymerization and layer deposition processes. However, considering cross-sections above 1.0 mm helps reduce defects and they remain intact during post-processing operations (42). During subsequent compression tests on Kresling cell samples, we observed a reduction in stiffness and peak loads of 30% after the second test and 50% after the third test. This can be attributed to crack initiation in thin creases made of rubbery photopolymers. This suggests material degradation in thin cross-sections made of the rubbery material after repeated loading cycles, potentially compromising its suitability for long-term applications. This observation highlights potential limitations in the reliability of this technique for experiments on multi-material Kresling cells, indicating potential long-term durability concerns. However, fabricating on a larger scale could be an option to overcome these manufacturing dimensional limitations, although it might result in higher material costs and longer working times.

4 Concluding remarks

We proposed alternatives to explore the untapped engineering potential of Kresling origami beyond traditional paper models. The advent of 3D printing has enabled the creation of complex multistable structures with programmable energy landscapes inspired by Kresling patterns. However, this approach also faces unique challenges related to manufacturing and material limitations, especially

at small scales and when addressing the visco-hyperelastic nature of photopolymers.

Our study emphasized the critical role of crease design in achieving reliable multistability in Kresling cells, highlighting overlooked parameters such as crease geometry and viscosity. By modifying the crease cross-section, we obtained diverse energy landscapes ranging from bistability, to monostability.

For instance, reducing the crease internal thickness s_i , through proposed reduction factors RF, by over 50% of the intact cross-section facilitated bistability, as confirmed by experimental validation that accounted for manufacturing limitations and scalability considerations. Rubbery creases with the highest relaxation modulus ($G_\infty \approx 0.855\text{MPa}$) compromised bistability, while those with lower relaxation moduli preserved it. In addition, the observed bistability remained over different time scales, including the initial, short- and long-term relaxation times regions. Consequently, we found that the difference in relaxation modulus had a greater impact on bistability than the time scale of analysis. Our results further indicate that the most significant changes in the energy landscape were primarily attributed to modifications in the geometrical parameters of the crease cross-section, which contributed to limiting the influence of visco-hyperelastic effects, especially in the configurations with the smallest cross-sections generated with a reduction factor RF=0.80.

Considering a monomaterial approach, stiffness variations achieved through voids in crease geometry improved the compression and expansion of Kresling cells and allowed energy storage to be tailored. Materials with intermediate stiffness ($E \approx 600\text{MPa}$) were identified as optimal for foldable, bistable designs, particularly oriented to micro-fabrication.

Moreover, we explored the role of creases in monostable Kresling assemblies by varying their stiffness. This allowed us to control the deformation of specific stories, enabling programmable energy landscapes and adjustable energy storage based on the inclusion of softer or stiffer creases.

In summary, our findings address key 3D printing challenges and offer potential for applications such as customized and scalable energy absorbers, actuators, and delivery robots that rely on compact and programmable energy landscapes. These configurations advance our understanding of Kresling-origami-inspired structures while also paving the way for future research.

5 Materials and Methods

5.1 Initial Sizing of Kresling cells

The geometrical parameters that define the initial sizing configuration of the Kresling cells were estimated using a five-parameters model (26), as further detailed in section [S.1.1](#) of Supplementary Materials and Methods. Considering a Kresling cylinder defined by top and bottom polygons with a number of sides $n=6$, under an axial displacement u , the total elastic stored energy of the creases U can be defined by the sum of the deformation strain U_b and the rotational springs U_s contribution of the peak and valley creases, by using the expressions:

$$U_b = \frac{1}{2}nK_{sb}(b - b_o)^2 + \frac{1}{2}nK_{sc}(c - c_o)^2, \quad (1)$$

$$U_s = \frac{1}{2}nK_a(\delta_a - \delta_{ao})^2 + \frac{1}{2}nK_b(\delta_b - \delta_{bo})^2 + \frac{1}{2}nK_c(\delta_c - \delta_{co})^2, \quad (2)$$

$$U = U_b + U_s \quad (3)$$

Here, K_{sb} and K_{sc} represent the stretching stiffness of the creases, while b and c denote the final lengths during the compression/expansion corresponding to the peaks and valleys, respectively. The original peak and valley lengths are denoted as b_o and c_o , respectively. The terms K_a, K_b , and K_c represent the rotational stiffness of the creases. The dihedral angles in the original configuration are $\delta_{ao}, \delta_{bo}, \delta_{co}$, while those in the folded configuration are $\delta_a, \delta_b, \delta_c$, corresponding to their respective creases. An iterative process was performed applying Eq. [3](#) to select the initial sizing configuration that theoretically leads to a second local minimum of energy when $\delta U / \delta u = 0$ (46, 47).

5.2 Parametric Design

The cylindrical Kresling cells were designed as solid bodies in Autodesk Inventor in 1:1 scale ($x1$), following the initial sizing configuration: polygons with $n=6$ sides, rotating at an initial angle $\theta_o = \pi/6$ with respect to each other, and an aspect ratio $h_o/r=1.75$. The panels were modeled with a small thickness value with respect to the initial height ($0.04 h_o \leq \bar{s} \leq 0.08 h_o$). In addition, rings were included at the top and bottom of the cylinders to ensure a uniform rotation of the upper and

lower polygons. Moreover, we created a small gap at the top and bottom intersections of the creases with the rings to prevent stress concentrations, as illustrated in the 3D Kresling cell renders from Fig. 3A.

In the Multi-material approach, the creases of the Kresling cells were parametrically designed with dimensional and geometrical variations. The dimensionless ratio w/s represents the creases width, w , variation relative to its thickness, s , ranging within $0.50 \leq w/s \leq 2.00$, and being gradually reduced considering the reduction factors $0.25 \leq RF \leq 0.80$. The generated configurations were obtained by combining the mentioned parameters and they are detailed in section S.1.2 of Supplementary Materials and Methods.

In the Mono-material approach, the Kresling cells were similarly designed following the initial sizing configuration and incorporating the creases design from the case C11- $RF=0.80$. The latter represents the most flexible crease with the lowest rotational stiffness ($\tilde{K}= 1.26 \times 10^{-5}$ N.mm/rad). The voids inclusions along the peaks and valleys, corresponded to a fraction of the total volume of their respective full creases, as explained in section 2.5. Thereby, multiple Kresling cell configurations for Multi-material and mono material approaches were exported as *.step and *.x_b Parasolid files, for the respective numerical simulations and 3D printing, respectively.

5.3 Numerical simulations and constitutive models

Quasi-static non-linear analyses were carried out in Abaqus/CAE Standard meshing the systems with quadratic tetrahedron C3D10MH elements due to the complexity of the geometry. This type of mesh contains 10 node quadratic tetrahedron with hybrid modified constant pressure elements. This choice was dictated by the hyperelastic nature of the rubbery material which is nearly incompressible. Tie constraints were assigned to the panels, creases, top and bottom ring surfaces to create a uniform contact among them. The defined boundary conditions at the bottom of the cylinder constrained all the displacements and the rotations. An imposed vertical displacement close to the one third of the initial height ($\approx 1/3 h_o$) was applied at the top.

Simultaneously, the rotation of the upper part was also released to simulate the natural twisted motion, characteristic of the Kresling patterns along with a compressive force. Furthermore, we remark that the quasi-static simulations were conducted using a VISCO step to capture the time-

dependent behavior of the visco-hyperelastic elements. The simulations proceeded until the target displacement was reached, ensuring that while the panels made initial contact during the folding process, overlapping was prevented. Further details are explained in section [S.1.3](#) of Supplementary Materials and Methods. Moreover, we incorporated calibrated material models obtained from their respective material characterization tests, as described in section [S.1.5](#) of Supplementary Materials and Methods. The components made of rigid materials, such as the panels and rings, were modeled with an elasto-plastic behavior. In contrast, flexible photopolymers were assigned to the creases, being initially characterized by a Neo-Hookean strain potential energy function described as follows:

$$U_N = C_{10}(\bar{I}_1 - 3) \quad (4)$$

where $C_{10}=G_o/2$, being G_o the instantaneous shear modulus and \bar{I}_1 is the first stretch invariant. This hyperelastic model assumes an almost incompressible material and was fitted to experimental data to find the C_{10} coefficients, which define the rate-independent behavior (48). Subsequently, the viscoelastic effects of the rubbery materials were then incorporated into the hyperelastic model. The Prony parameters dimensionless weight g_i and relaxation time τ_i characterize the time-dependent behavior associated with viscosity (49). They were determined by a non-linear regression analysis by fitting them to the relaxation test data, as detailed in section [S.1.6](#) of Supplementary Materials and Methods. We then applied the obtained Prony parameters to the constants within the strain energy function $U_N(t)$, which is defined by the instantaneous constant C_{10}^o , and the visco-hyperelastic relaxation function can be expressed as follows:

$$U_N(t) = C_{10}^o \left(1 - \sum_{i=1}^N g_i (1 - e^{-t/\tau_i}) \right) \quad (5)$$

In the context of Polyjet photopolymers, the selected rigid material for the panels in all the numerical simulations of multi-material cases was VeroBlack (VB). Regarding the flexible creases, the rubbery digital material DM60 was used for the first parametric study (section [2.1](#)). In subsequent analyses, we included additional rubbery photopolymers with different relaxation moduli and viscosity than DM60, such as Agilus30 (AG30) and digital materials DM70, DM85, and DM95, to evaluate and predict the effects of viscosity on bistability (section [2.3](#)). The duration of each numerical simulation using the VISCO step, was set equal to the initial, short-term and long-term relaxation times exhibited by the different rubbery materials, based on their relaxation times τ_i from

the Prony series. For the mono-material approach, flexible photopolymers used in other 3D printing techniques were also considered, including Origin 402 (Direct Light Processing), IP-PDMS and UTL-BMF (Two-photon polymerization for micro-fabrication).

5.4 Fabrication of Multi-material Kresling cells

The Kresling cell samples were fabricated following the framework of Polyjet multi-material technique. It is important to remark that cross-sections of structural elements lower than 1.0 mm demand special attention during the Polyjet process. They are prone to exhibit defects and demand extremely careful post-processing operations. For this reason, the printed Kresling cells were scaled three times to make the printing feasible, maintaining the ratios and proportions previously detailed in the parametric design section [5.2](#), video S6 and section [S.1.2](#) of Supplementary Materials and Methods. Based on the materials we used in the numerical simulations, the panels were fabricated with VeroBlack (VB). For the creases, the following flexible materials were employed in the different Kresling cells: AG30, DM60, DM70, DM85 and DM95.

5.5 Experimental validation

The 3D CAD models were generated in Autodesk Inventor, to be subsequently printed in a Stratasys J750 printer series. The selected printing setting was High-Mix mode with a layer resolution thickness of 27 microns and glossy surface finishing. The majority of the supports grids made of SUP706B material surrounding the printed Kresling cells were manually removed, and briefly rinsed in water for less than five minutes. A prolonged contact between small elements or multi-material interfaces, lower than 1.0 mm cross-section, with water or alkaline solutions lead to a premature breakage and detachment. Further details on the fabrication of 3D printed Kresling cells protocol are presented in section [S.1.7](#) of Supplementary Materials and Methods. A series of quasi-static experiments were carried on the 3D printed Kresling cells to validate the numerical simulations results. A compression load was applied at the top with an imposed displacement of approximately $u \approx 1/3 h_o$. The experimental setup, described detail in section [S.1.8](#) - Fig. [S10](#) of Supplementary Materials and Methods, consists on a fixture that resembles free rotation assigned to the top of the sample, with a fixed bottom fixture to prevent displacements and rotations. Thus,

replicating the natural twist under compression inherent in Kresling patterns kinematics (26). The connections between the sample and the setup were implemented in two different systems: (i) A female-male pinned system, and (ii) Use of magnets to prevent the sliding of the samples. The cross-head testing speed was 0.1 mm/sec, which can be considered sufficiently slow to capture viscosity effect (relaxation time $\tau_i^* = 180$ s), as well as the most representative bistable behavior according to numerical predictions across different time scales.

5.6 Microscopic characterization of 3D printed creases

The real dimensions of the 3D printed samples were determined via a stereo microscope (Nikon SMZ800) equipped with an ED Plan 1.5x lens and with a DS-Ri2 camera. The analyzed creases belong to the configurations presented in case C8 with gradual reductions between $0.25 \leq RF \leq 0.80$. We compared the mean values of the real measurements of the 3D printed Kresling cells, versus the exact measurements of the CAD models, as detailed in section [S.1.10](#) of Supplementary Materials and Methods. Thus, we determined the mean percentage error, M_{PE} (%) between the dimensions from the tested samples and those used in the numerical simulations. Hence, this estimated error was incorporated to update the analyzed geometrical configurations and considering the loss of dimensional accuracy attributed to the Polyjet printing process.

References and Notes

1. D. Misseroni, *et al.*, Origami engineering. *Nature Reviews Methods Primers* **4** (1), 40 (2024).
2. J. Kaufmann, P. Bhovad, S. Li, Harnessing the multistability of kresling origami for reconfigurable articulation in soft robotic arms. *Soft Robotics* **9** (2), 212–223 (2022).
3. P. Bhovad, J. Kaufmann, S. Li, Peristaltic locomotion without digital controllers: Exploiting multi-stability in origami to coordinate robotic motion. *Extreme Mechanics Letters* **32**, 100552 (2019).
4. Q. Ze, *et al.*, Soft robotic origami crawler. *Science Advances* **8** (13), eabm7834 (2022).

5. L. S. Novelino, Q. Ze, S. Wu, G. H. Paulino, R. Zhao, Untethered control of functional origami microrobots with distributed actuation. *Proceedings of the National Academy of Sciences* **117** (39), 24096–24101 (2020).
6. S. Wu, *et al.*, Stretchable origami robotic arm with omnidirectional bending and twisting. *Proceedings of the National Academy of Sciences* **118** (36), e2110023118 (2021).
7. X. Wang, *et al.*, Multi-triangles cylindrical origami and inspired metamaterials with tunable stiffness and stretchable robotic arm. *PNAS Nexus* **2** (4), pgad098 (2023).
8. S. Wu, T. Zhao, Y. Zhu, G. H. Paulino, Modular multi-degree-of-freedom soft origami robots with reprogrammable electrothermal actuation. *Proceedings of the National Academy of Sciences* **121** (20), e2322625121 (2024).
9. Y. Yao, G. Li, X. Ning, Origami electronic membranes as highly shape-morphable mechanical and environmental sensing systems. *Extreme Mechanics Letters* **73**, 102264 (2024).
10. H. Yasuda, *et al.*, Origami-based impact mitigation via rarefaction solitary wave creation. *Science advances* **5** (5), eaau2835 (2019).
11. J. Li, Y. Chen, X. Feng, J. Feng, P. Sareh, Computational modeling and energy absorption behavior of thin-walled tubes with the Kresling origami pattern. *Journal of the International Association for Shell and Spatial Structures* **62** (2), 71–81 (2021).
12. J. Cai, X. Deng, Y. Zhang, J. Feng, Y. Zhou, Folding behavior of a foldable prismatic mast with kresling origami pattern. *Journal of Mechanisms and Robotics* **8** (3), 031004 (2016).
13. H. Yang, *et al.*, 3D-printable Kresling-embedded honeycomb metamaterials with optimized energy absorption capability. *Smart Materials and Structures* **33** (12), 125008 (2024).
14. Z. Zhai, Y. Wang, H. Jiang, Origami-inspired, on-demand deployable and collapsible mechanical metamaterials with tunable stiffness. *Proceedings of the National Academy of Sciences* **115** (9), 2032–2037 (2018).
15. V. Agarwal, K. Wang, On the nonlinear dynamics of a Kresling-pattern origami under harmonic force excitation. *Extreme Mechanics Letters* **52**, 101653 (2022).

16. S. Li, Y. Miyazawa, K. Yamaguchi, P. G. Kevrekidis, J. Yang, Geometry-informed dynamic mode decomposition in Kresling origami dynamics. *Extreme Mechanics Letters* **64**, 102082 (2023).
17. Y. Wang, X. Zhang, S. Zhu, Highly intensive and controllable supratransmission in a Kresling-origami metastructure. *Extreme Mechanics Letters* **59**, 101964 (2023).
18. Z.-L. Xu, D.-F. Wang, T. Tachi, K.-C. Chuang, An origami longitudinal–torsional wave converter. *Extreme Mechanics Letters* **51**, 101570 (2022).
19. B. Kresling, Natural twist buckling in shells: from the hawkmoth’s bellows to the deployable Kresling-pattern and cylindrical Miura-ori, in *Proceedings of the 6th International Conference on Computation of Shell and Spatial Structures IASS-IACM* (2008), p. 4.
20. B. Kresling, Folded tubes as compared to kikko (‘tortoise-shell55) bamboo, in *Origami* (Barnes Noble), p. 197 (2002).
21. Q. Zhang, J. Cai, M. Li, J. Feng, Bistable behaviour of a deployable cylinder with Kresling pattern, in *Proceedings of the 7th International Meeting on Origami in Science, Mathematics and Education (7OSME)*, Oxford, UK (2018), pp. 4–7.
22. S. V. Georgakopoulos, *et al.*, Origami antennas. *IEEE Open Journal of Antennas and Propagation* **2**, 1020–1043 (2021).
23. X. Liu, S. Yao, S. V. Georgakopoulos, Mode reconfigurable bistable spiral antenna based on kresling origami, in *2017 IEEE International Symposium on Antennas and Propagation & USNC/URSI National Radio Science Meeting (IEEE)* (2017), pp. 413–414.
24. K. Liu, G. Paulino, Nonlinear mechanics of non-rigid origami: an efficient computational approach. *Proceedings of the Royal Society A: Mathematical, Physical and Engineering Sciences* **473** (2206), 20170348 (2017).
25. Z. Li, N. Kidambi, L. Wang, K.-W. Wang, Uncovering rotational multifunctionalities of coupled Kresling modular structures. *Extreme Mechanics Letters* **39**, 100795 (2020).

26. S. Zang, D. Misseroni, T. Zhao, G. H. Paulino, Kresling origami mechanics explained: Experiments and theory. *Journal of the Mechanics and Physics of Solids* p. 105630 (2024).
27. X. Wang, H. Qu, S. Guo, Tristable property and the high stiffness analysis of Kresling pattern origami. *International Journal of Mechanical Sciences* **256**, 108515 (2023).
28. D. Dureisseix, An overview of mechanisms and patterns with origami. *International Journal of Space Structures* **27** (1), 1–14 (2012).
29. A. S. Dalaq, M. F. Daqaq, Experimentally-validated computational modeling and characterization of the quasi-static behavior of functional 3D-printed origami-inspired springs. *Materials & Design* **216**, 110541 (2022).
30. A. S. Dalaq, S. Khazaaleh, M. F. Daqaq, An origami-inspired design of highly efficient cellular cushion materials. *Applied Materials Today* **32**, 101835 (2023).
31. R. Masana, M. F. Daqaq, Quasi-static behavior of a pair of serially-connected Kresling Origami springs. *International Journal of Solids and Structures* **298**, 112877 (2024).
32. Q. Liu, *et al.*, Stiffness-Tunable Origami Structures via Multimaterial Three-Dimensional Printing. *Acta Mechanica Solida Sinica* pp. 1–12 (2023).
33. D. Melancon, A. E. Forte, L. M. Kamp, B. Gorissen, K. Bertoldi, Inflatable origami: Multimodal deformation via multistability. *Advanced Functional Materials* **32** (35), 2201891 (2022).
34. H. Ye, *et al.*, Multimaterial 3D printed self-locking thick-panel origami metamaterials. *Nature communications* **14** (1), 1607 (2023).
35. Y. X. Mak, A. Dijkshoorn, M. Abayazid, Design Methodology for a 3D Printable Multi-Degree of Freedom Soft Actuator Using Geometric Origami Patterns. *Advanced Intelligent Systems* **6** (6), 2300666 (2024).
36. C. Zhang, *et al.*, Plug & play origami modules with all-purpose deformation modes. *Nature Communications* **14** (1), 4329 (2023).
37. M. Moshtaghadeh, E. Izadpanahi, P. Mardanpour, Prediction of fatigue life of a flexible foldable origami antenna with Kresling pattern. *Engineering Structures* **251**, 113399 (2022).

38. H. Cho, *et al.*, Engineering the mechanics of heterogeneous soft crystals. *Advanced Functional Materials* **26** (38), 6938–6949 (2016).
39. F. F. Abayazid, M. Ghajari, Material characterisation of additively manufactured elastomers at different strain rates and build orientations. *Additive Manufacturing* **33**, 101160 (2020).
40. Ultimaker, How to design for FFF 3D printing, Ultimaker, <https://ultimaker.com/wp-content/uploads/2024/06/How-to-design-for-FFF-1.pdf>.
41. Stratasys, Four Key Factors for a Balanced Design, Stratasys, <https://www.stratasys.com/en/stratasysdirect/resources/articles/3d-printing-balanced-design-key-factors/>.
42. S. Mora, N. M. Pugno, D. Misseroni, 3D printed architected lattice structures by material jetting. *Materials Today* (2022).
43. Y. Chi, *et al.*, Bistable and multistable actuators for soft robots: Structures, materials, and functionalities. *Advanced Materials* **34** (19), 2110384 (2022).
44. D. Bigoni, *Nonlinear solid mechanics: bifurcation theory and material instability* (Cambridge University Press) (2012).
45. BMF, UTL resin datasheet, BMF, <https://ultimaker.com/wp-content/uploads/2024/06/How-to-design-for-FFF-1.pdf>.
46. R. Masana, M. F. Daqaq, Equilibria and bifurcations of a foldable paper-based spring inspired by Kresling-pattern origami. *Physical Review E* **100** (6), 063001 (2019).
47. H. Yasuda, T. Tachi, M. Lee, J. Yang, Origami-based tunable truss structures for non-volatile mechanical memory operation. *Nature Communications* **8** (1), 1–7 (2017).
48. Dassault Systèmes, *Abaqus Documentation, Hyperelastic behavior of rubberlike materials* (2010), version 6.10.
49. C. Tzikang, *Determining a Prony series for a viscoelastic material from time varying strain data*, Tech. rep., NASA (2000).

Acknowledgments

Funding: SM co-funded by the European Union under Horizon Europe Programme, project 'SUBBIMATT - Sustainable, Biobased and Bio-Inspired Materials for Smart Technical Textiles', HE Grant Agreement 101129911 — SUBBIMATT. NMP is supported by the European Union BOHEME prjct, H2020 FET Open programme, GA 863179. DM is funded by the European Union, project 'S-FOAM – Self-Foldable Origami-Architected Metamaterials', ERC grant HE GA 101086644 S-FOAM.

Author contributions: Conceptualization: S.M, D.M. Methodology: S.M, D.M. Data acquisition & Formal analysis: S.M. Numerical simulations: S.M. Experiments & prototyping: S.M, D.M. Supervision: D.M., N.M.P. Writing—original draft: S.M, D.M. Writing—review & editing: S.M, D.M, N.M.P. Funding acquisition: D.M, N.M.P.

Competing interests: There are no competing interests to declare.

Data and materials availability: All the data, physical samples, simulation outputs have been obtain at the Laboratory of Design of Metamaterials and Structures, DICAM, University of Trento. All the data that supports the findings of this research can be downloaded here.

Supplementary materials

Materials and Methods

Supplementary Text

Figs. S1 to S34

Tables S1 to S2

References (7-49)

Video S1 to S6